Stress effect on the leakage current distribution of ferroelectric $Al_{0.7}Sc_{0.3}N$ across the wafer

Wanwang Yang,[1] Li Chen,[2] Minghua Li,[2] Fei Liu,[1] Xiaoyan Liu,[1] Chen Liu,[2, a)] and Jinfeng Kang[1, b)]

[1)] *School of Integrated Circuits, Peking University, Beijing, 100871, China*

[2)] *Institute of Microelectronics, Agency for Science, Technology and Research, Singapore 138634, Singapore*

(Dated: 5 September 2023)

This study presents an investigation into the stress effect on the leakage current in ferroelectric $Al_{0.7}Sc_{0.3}N$ films by experiments and density functional theory (DFT) computations. The experiments are based on 8-inch 100nm $Al_{0.7}Sc_{0.3}N$ films obtained from pulsed DC co-sputter deposition technology, which exhibit non-uniform compressive in-plane stress across the wafers and similar distributions of leakage current, suggesting close dependence between each other. DFT computations revealed that stress affects leakage current in two ways: the level of traps introduced by nitrogen vacancy and the formation energy of nitrogen vacancy in $Al_{0.7}Sc_{0.3}N$. By considering both factors, the leakage current of $Al_{0.7}Sc_{0.3}N$ films increases with larger compressive in-plane stress, as observed in the experimental results. Additionally, the DFT calculation results indicated that the leakage current is more sensitive to compressive stress compared to the tensile and the minimum leakage current can be obtained with neutral in-plane stress. These findings provide a guideline for stress engineering to optimize the AlScN-based ferroelectric devices.

[a)] Authors to whom correspondence should be addressed: Liu_Chen@ime.a-star.edu.sg
[b)] Authors to whom correspondence should be addressed: kangjf@pku.edu.cn

Aluminum nitride (AlN), with a wurtzite structure, is a well-known piezoelectric material.[1–4] After Akiyama found a tremendous enhancement of piezoelectric response in the Sc-alloyed wurtzite $Al_{1-x}Sc_xN$,[5] this ternary III-nitride alloy offers good prospects for high-frequency filtering,[6–11] energy harvesting applications,[12–14] and other piezoelectric devices.[15–17] Recently, $Al_{1-x}Sc_xN$ was demonstrated to be ferroelectric with a large switchable polarization, steep switching, and high Curie temperature,[18–22] which has drawn great research interest.

The improved piezoelectric performance and unique ferroelectric behavior, as well as the high compatibility with both complementary metal-oxide-semiconductor (CMOS) and III-nitride technology, make $Al_{1-x}Sc_xN$ a promising material for multi-functional devices.[19,23–30] However, the large coercive field and leakage current, which lead to higher operation voltages, larger power consumption, and worse reliability compared with other ferroelectric materials, hinder the practical integration and effective applications of $Al_{1-x}Sc_xN$-based devices.[18,19,31–34] The large coercive field of $Al_{1-x}Sc_xN$ is commonly believed to arise from the huge crystal anisotropy,[26,32,35] and the high leakage current is attributed to the presence of defects, especially nitrogen vacancies (V_N) in $Al_{1-x}Sc_xN$.[19,29,36,37] Due to the widespread presence of in-plane stress in ferroelectric $Al_{1-x}Sc_xN$ films, numerous studies have been conducted to explore the coercive field and remnant polarization modification using stress engineering,[33,35,38,39] but there is little research on the effect of stress on the leakage current, which is also important for future applications.

In this work, by experiments and theoretical calculations, the effect of stress on leakage current in ferroelectric $Al_{0.7}Sc_{0.3}N$ thin films is elucidated. In experiments, the wafer-level distribution of the leakage current and localized in-plane stress on an 8-inch 100nm $Al_{0.7}Sc_{0.3}N$ thin film are systematically examined and compared, revealing the correlation between them. To explain the observed correlation, through density functional theory (DFT) computations, we first calculated the formation energies of various defects and confirmed that V_N is the dominant one in $Al_{0.7}Sc_{0.3}N$, which introduces four defect levels within the band gap and leads to the Poole-Frenkel (P-F) emission as the major leakage.[19,40] Then we focused on the effect of in-plane stress on the V_N, including the trap levels and formation energy. The results show that the shallowest trap energy level increases slowly with increasing compressive in-plane stress, while the formation energy changes much more rapidly and decreases (increases) as the compressive (tensile) in-plane stress escalates. By considering these two factors jointly, the leakage issue of $Al_{0.7}Sc_{0.3}N$ becomes severer with incremental compressive in-plane stress, which is consistent with the experiments. Finally, theoretical results indicate that the leakage current is more sensitive to compressive in-plane stress

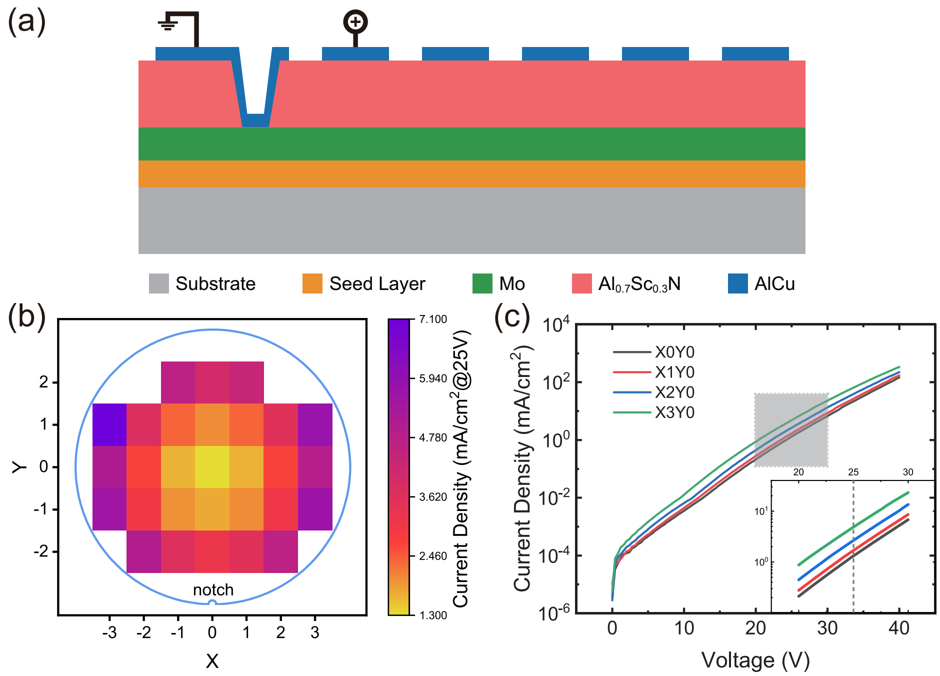

FIG. 1. (a) Schematic of AlCu/$Al_{0.7}Sc_{0.3}N$/Mo devices on an 8-inch wafer. A small portion of $Al_{0.7}Sc_{0.3}N$ has been etched to form the via accessing the bottom electrode shared by the devices. (b) Leakage current distribution of the MFM devices with 25V positive bias after polarization poling with +40V DC bias. (c) A series of I-V curves of the devices located in different dies in (b), from the center region (X0Y0) to the edge region (X3Y0). The inset is an enlarged view of the gray box area in (c).

compared to tensile stress, and the neutral stress should be the target for leakage reduction.

The schematic diagram of AlCu/$Al_{0.7}Sc_{0.3}N$/Mo devices on an 8-inch wafer is illustrated in Fig. 1(a). AlN seed layer and 50nm Mo bottom electrode (BE) were deposited by sputtering on the Si substrate. Then 100nm $Al_{0.7}Sc_{0.3}N$ film was grown by reactive pulsed DC co-sputtering from dual targets of Al and Sc in N_2 atmosphere. Wafer-level film stress was measured and calculated with the Stoney equation. After stress measurement, a small portion of the AlScN film was etched to form the via which exposes the Mo BE, followed by 100nm AlCu top electrode (TE) layer deposition using lift-off. Metal/ferroelectric/metal (MFM) capacitors were thus constructed with a device area of $10^4 \mu m^2$. The Mo BE, which is accessed by the via, is shared by all the

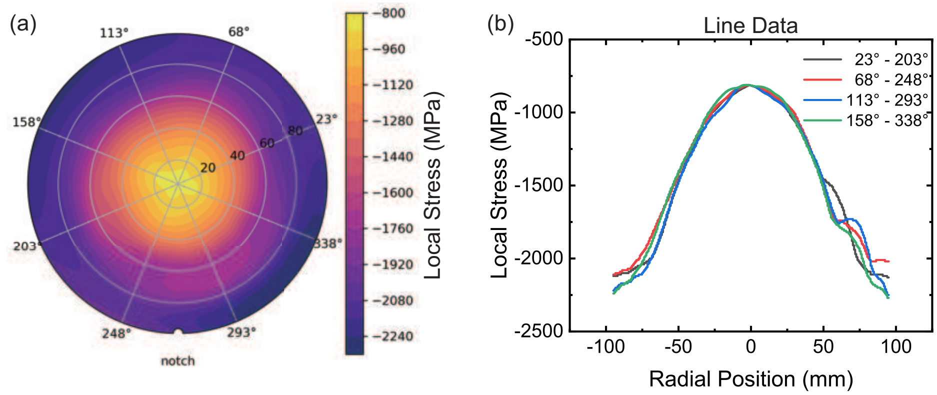

FIG. 2. Local in-plane stress of the $Al_{0.7}Sc_{0.3}N$ thin film. (a) Heat map of the local stress distribution across the 8-inch wafer. (b) Local stress varies as a function of the radial position along the gray straight lines marked in (a).

MFM devices. To avoid the impact of polarization direction on the leakage current, for all the MFM devices, the leakage current was performed after polarization poling with +40V (4MV/cm) DC bias, and the current density was obtained with 25V positive bias applied on the TE and BE connected to ground.

Fig. 1(b) shows the distribution of leakage current of the ferroelectric $Al_{0.7}Sc_{0.3}N$-based MFM devices on the 8-inch wafer and Fig. 1(c) presents a series of I-V curves of the devices located in different dies, from the center region (X0Y0) to the edge region (X3Y0). The measurement results reveal a non-uniform distribution of leakage current across the wafer. A nearly central symmetric pattern radiates from the center to the edge of the wafer. Within the central die, the MFM devices experience the lowest leakage current. The current increases from the center of the wafer to the edge, reaching up to five times the value of the center die.

In order to explore the correlation of this non-uniform leakage current distribution with the in-plane stress, the distribution of the stress of the $Al_{0.7}Sc_{0.3}N$ thin films has been measured. As illustrated in Fig. 2, the whole 100nm $Al_{0.7}Sc_{0.3}N$ thin film is under compressive in-plane stress, and the central region is under less compressive stress around -800 MPa, while the edge is under higher compressive stress around -2300 MPa. It should be noted that the in-plane stress of the sputtered thin film is observed to exhibit variations along the thickness direction[41], progressively relaxing from highly compressive as it approaches the surface. Since this thickness-dependency applies to the whole wafer, the stress on the upper surface of $Al_{0.7}Sc_{0.3}N$ film was measured and represented the local in-plane stress. In this way, a qualitative stress distribution across the wafer was obtained. Comparing under the same standard, the stress distribution could represent the relative stress relationship in the devices. The in-plane stress is widespread in ferroelectric $Al_{1-x}Sc_xN$ films and could be adjusted by the fabrication conditions, such as epitaxial mismatch strain and thermal strain from substrates and electrodes,[32,42] partial pressure of the sputtering gas,[18,33] sputtering power and growth temperature,[33,34] and the electrical termination of the sputtering targets.[43] The inhomogeneity of local stress can be attributed to the difference in energy of ion bombardment across the wafer during fabrication.[44] Similar to the non-uniform distribution of leakage current, the local stress also presents a nearly central symmetric distribution, which is illustrated by the heat map combined with the four cross-line data in Fig. 2. These results indicate an obvious proportional dependence of the leakage current on compressive in-plane stress of the $Al_{1-x}Sc_xN$ film. This relationship is visualized in Fig. 3, which collects the leakage current data from Fig. 1 (b) and stress data from Fig. 2, presenting that the leakage current increases with larger compressive in-plane stress. To further prove the universality of this correlation in $Al_{1-x}Sc_xN$ materials, the measured leakage current and stress maps of another 8-inch wafer, with 100nm thickness sputtered $Al_{0.8}Sc_{0.2}N$ thin film on it, were provided in the supplementary material (Fig. S1). Though the $Al_{0.8}Sc_{0.2}N$ thin film is under smaller in-plane stress, the leakage current and local stress distributions are also nearly central symmetric, with leakage increasing at larger compressive stress regions, similar to $Al_{0.7}Sc_{0.3}N$ thin film.

Many possible factors may impact the leakage current in thin films, including point defects, film crystallinity, grain boundary, domain structure, impurities, and so on. As for $Al_{1-x}Sc_xN$ films, the source of the leakage current has been systematically investigated by previous works,[19,29,34,36,37] and it is widely acknowledged that the leakage current may originate from point defects. To address the concern about the uniformity of film thickness and quality, the transmission electron microscope (TEM) and energy dispersive X-Ray spectroscopy (EDX) characterizations were carried out with results shown in Fig. S2 and Table S1. Thus, the point defect-based leakage mechanism and the corresponding stress effect should be considered first.

Starting from this point, a series of DFT calculations for point defects were carried out to gain more insights into the underlying relationship between stress and leakage current of ferroelectric $Al_{0.7}Sc_{0.3}N$ thin films. The wurtzite $Al_{0.6875}Sc_{0.3125}N$ solid solution atomic crystal model was constructed based on special quasirandom structure (SQS) method[45,46], a genearal method to

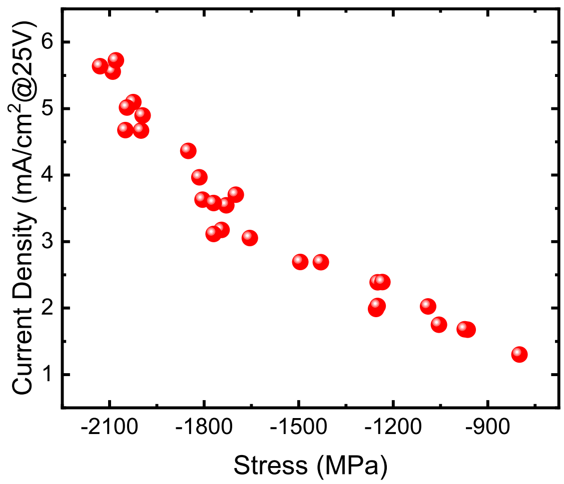

FIG. 3. The relationship between leakage current of the MFM devices and stress of the $Al_{0.7}Sc_{0.3}N$ thin film.

use a specific structure to represent the randomness of alloy material systems in first-principles calculations, which implemented in the mcsqs code[47] of the Alloy Theoretic Automated Toolkit (ATAT).[48] This $Al_{0.6875}Sc_{0.3125}N$ SQS contains 44 Al, 20 Sc, and 64 N atoms within a 4×4×2 supercell composed of 32 wurtzite unit cells. DFT calculations were performed using the generalized gradient approximations of Perdew-Burke-Ernzerhof GGA-PBE exchange-correlation functional and the projector-augmented wave (PAW) pseudo-potentials,[49–51] implemented in the Vienna Ab initio Simulation Package (VASP) code.[52] The valence electron configurations of Al, Sc, and N were set as $3s^23p^1$, $3s^23p^64s^23d^1$, and $2s^22p^3$, respectively. The cutoff energy was set to 520 eV for the plane-wave basis set, and the Γ-centered k-points mesh was created with a resolution of $2\pi\times0.04$ Å^{-1}. All structures were fully relaxed, including lattice vectors (except the structures under in-plane stress) and atom positions, with a force criterion of 0.01 eV/Å, and the convergence for the self-consistent field (SCF) calculations was set to 10^{-6} eV. The structural models in this work were visualized by the Visualization for Electronic and STructural Analysis (VESTA) program.[53]

We first calculated the formation energies of various defects in a SQS $Al_{0.6875}Sc_{0.3125}N$ with a 4×4×2 supercell, as illustrated in Fig. 4(a). The formation energy E_{form} of the defect α in the

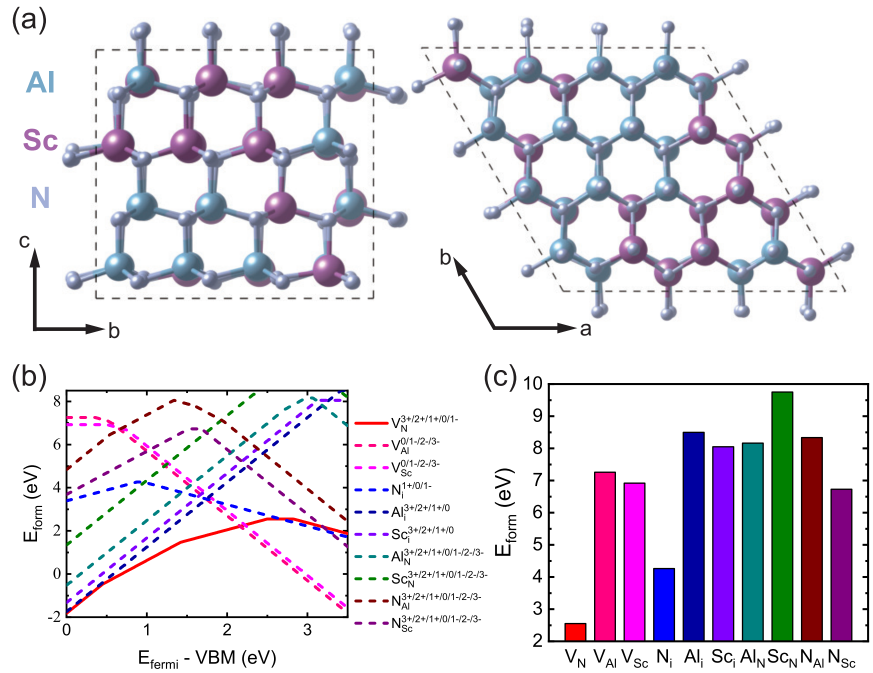

FIG. 4. (a) Side view (left) and top view (right) of the SQS of wurtzite $Al_{0.6875}Sc_{0.3125}N$ with a $4\times4\times2$ supercell. (b) Formation energies of various defects inside the SQS $Al_{0.6875}Sc_{0.3125}N$ as a function of the Fermi energy above VBM, including N vacancy (V_N), Al vacancy (V_{Al}), Sc vacancy (V_{Sc}), interstitial N (N_i), interstitial Al (Al_i), interstitial Sc (Sc_i), antisite Al at N (Al_N), antisite Sc at N (Sc_N), antisite N at Al (N_{Al}), antisite N at Sc (N_{Sc}). The superscripts represent the charge state. Each curve represents one type of defect and consists of several segments, and each segment represents the charge state with the lowest E_{form} at this E_{fermi} (the slope determined by the charge state). The E_{form} of V_N is plotted with solid line, and the E_{form} of other defects are plotted with dashed lines for legibility. (c) Formation energies of various neutral defects in $Al_{0.6875}Sc_{0.3125}N$. Clearly, the V_N has the lowest formation energy and is most likely to be generated in $Al_{0.6875}Sc_{0.3125}N$.

charge state q is defined as[54]

$$E_{form}(\alpha^q, E_{fermi}) = E_{tot}(\alpha^q) - E_{tot}(bulk) - \sum_i n_i \mu_i + qE_{fermi}. \quad (1)$$

$E_{tot}(\alpha^q)$ is the total energy derived from the DFT computation of the SQS supercell containing the defect, and $E_{tot}(bulk)$ is the total energy of the defect-free SQS. n_i is the number of type i atoms added or removed from bulk to form the defect, and μ_i is the corresponding chemical potential of this species. E_{fermi} is the Fermi energy, which means the chemical potential of the electrons. Here, we take an intermediate condition of the chemical environment between Al-rich condition and N-rich condition, i.e.

$$\begin{cases} \mu_{\mathrm{Al}} = \frac{1}{2}\left\{[E_{tot}(\mathrm{Al})] + \frac{1}{2}[E_{tot}(\mathrm{AlN}) - E_{tot}(\mathrm{N_2})]\right\} \\ \mu_{\mathrm{N}} = \frac{1}{2}\left\{\left[\frac{1}{2}E_{tot}(\mathrm{AlN}) - E_{tot}(\mathrm{Al})\right] + \frac{1}{2}[E_{tot}(\mathrm{N_2})]\right\} \\ \mu_{\mathrm{Sc}} = E_{tot}(\mathrm{ScN}) - \mu_{\mathrm{N}} \end{cases}, \tag{2}$$

where $E_{tot}(\mathrm{Al})$, $E_{tot}(\mathrm{AlN})$, $E_{tot}(\mathrm{N_2})$, and $E_{tot}(\mathrm{ScN})$ are the total energies of a one-atom unit of cubic Al, a four-atom unit of wurtzite AlN, a N_2 gas molecule, and a two-atom unit of rock salt ScN, respectively.

All the possible N/Sc/Al defect types (vacancies, interstitials, and antisites), charge states, and relative sites in the SQS $Al_{0.6875}Sc_{0.3125}N$ supercell have been taken into account. The lowest formation energy of each defect type has been filtered out. The formation energies of these defects in different charge states were calculated as a function of E_{fermi}. As shown in Fig. 4(b), the most favorable charge state for a defect, possessing the lowest formation energy, changes as E_{fermi} varies between valance band maximum (VBM) and conduction band minimum (CBM). Each curve represents one type of defect and consists of several segments, and each segment represents the charge state with the lowest E_{form} at this E_{fermi} (the slope determined by the charge state). The Fermi energy at which the formation energies of charge state q_1 and q_2 are equivalent is identified as the transition level, alternatively referred to as the defect level $\varepsilon(q_1/q_2)$,[54]

$$\varepsilon(q_1/q_2) = \frac{E_{form}(\alpha^{q_1},0) - E_{form}(\alpha^{q_2},0)}{q_2 - q_1}. \tag{3}$$

It is clearly illustrated in Fig. 4(b) that among most range of the Fermi energy, the V_N possesses the lowest formation energy, especially when the Fermi energy is around the center of the band gap. Meanwhile, the formation of V_N introduces four defect levels into the band gap, which could act as trapping centers for electrons and lead to an increment of leakage current.

Due to the difficulty of determining the accurate Fermi energy and the charge state, the formation energies of these defects in neutral charge states, which are independent of the Fermi energy as shown in Eq. (1) with $q = 0$, have been depicted in Fig. 4(c) as a supplement to describe the thermodynamic stability of the defect in AlScN. The results show that V_N has the lowest formation energy of 2.55 eV, which is around half of the second lowest formation energy (N_i), meaning V_N is supposed to be the predominant one among various defects. Therefore, we focused on the effect of stress on V_N.

Here, we took the P-F emission behavior as the dominant mechanism of leakage current in $Al_{1-x}Sc_xN$ thin films, which has been reported in our previous work,[19] based on the same film thickness and Sc concentration. This mechanism was verified by the linear relationship between ln(I/V) and $V^{1/2}$, as shown in Fig. S3 in the supplementary material. In the P-F emission mechanism, trap energy barrier $e\phi_t$ and defect concentration $c(\alpha)$ are affected by stress. The trap energy barrier could be obtained from electronic band structure combined with defect level, as

$$e\phi_t = \mathrm{CBM} - \varepsilon(q_1/q_2), \tag{4}$$

and the defect concentration could be described based on the formation energy, as

$$c(\alpha) \propto \exp\left(-\frac{E_{form}(\alpha)}{k_B T}\right), \tag{5}$$

where k_B is the Boltzmann constant and T is the temperature.

To simulate the in-plane stress prevailing in sputter deposited $Al_{1-x}Sc_xN$ thin films, an equibiaxial in-plane strain was imposed on the SQS $Al_{0.6875}Sc_{0.3125}N$ through a constrained relaxation. The in-plane lattice vectors [1000] and [0100] were fixed with the same rescaling factor in the constrained relaxation, while the lattice along [0001] direction and all atoms in the strained structure were allowed to relax.[55,56] The in-plane strain was set between -0.02 to 0.02, with an interval of 0.002, based on the range of local stress displayed in Fig. 2 and the modulus of $Al_{1-x}Sc_xN$, while the out-of-plane strain was relaxed with opposite polarity to the applied in-plane strain, as shown in Fig. S4.

Fig. 5(a) presents the CBM of $Al_{0.6875}Sc_{0.3125}N$ and the four defect levels induced by V_N, relative to the VBM of bulk, as functions of the in-plane strain. The missing data points of defect level 4 with strain above 0.15 is due to the structural instability of $Al_{0.6875}Sc_{0.3125}N$ with V_N^{1-} undergoing huge in-plane strain. In Fig. 5(a), it is obviously shown that the CBM and defect levels 4 present similar monotonic trends, declining with larger strain (numerical), while the CBM decreases at a faster rate, especially with tensile strain. Then, the trap energy barriers $e\phi_t$ were extracted via Eq. 4 and plotted in Fig. 5(b). The $e\phi_t$s of all the traps decrease monotonically with increasing strain. A possible explanation is that these trap states are spatially localized rather

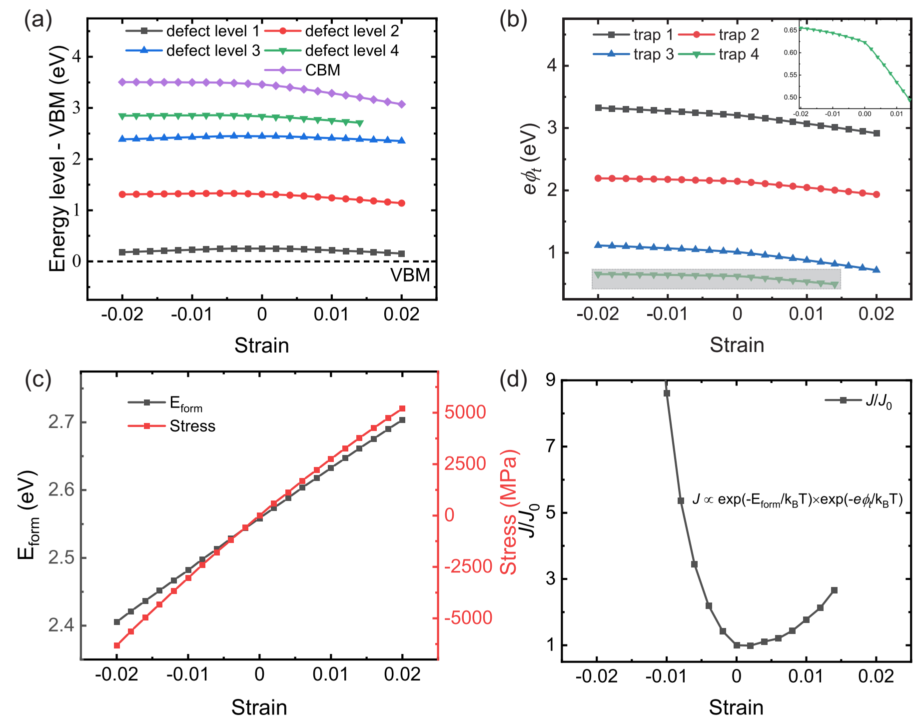

FIG. 5. Effect of in-plane stress. (a) Electronic band edge of $Al_{0.6875}Sc_{0.3125}N$ and defect levels introduced by V_N, referenced to the VBM. (b) Corresponding trap energy barriers $e\phi_t$. The inset is an enlarged view of the gray box area in (b), illustrating the trend of the shallowest trap energy barrier. (c) Formation energy (left axis) of V_N in $Al_{0.6875}Sc_{0.3125}N$ and in-plane stress of $Al_{0.6875}Sc_{0.3125}N$. (d) Normalized P-F emission leakage current J/J_0, where J_0 is the leakage without in-plane stress.

than coupled to the host system, resulting in a fairly weaker dependence on the lattice constant compared to the CBM.[54] The shallowest trap energy barrier $e\phi_{t_4}$, dominating the P-F emission leakage over other trap levels, is around 0.6 eV, comparable to the reported results in Ref.19 and 40, and as clearly illustrated by the inset, $e\phi_{t_4}$ decreases rapidly after the transition from compressive to tensile in-plane strain.

The effect of in-plane strain on the formation energy of V_N in $Al_{0.6875}Sc_{0.3125}N$ and the corresponding in-plane stress are depicted in Fig. 5(c), both exhibiting a linear relationship with in-plane strain. Based on the P-F emission mechanism and results of Figs. 5(b,c), it is evident that with increasing compressive in-plane stress, on the one hand, higher trap energy barrier $e\phi_{t_4}$ could decrease the leakage current, but on the other hand, lower formation energy of V_N brings higher defect concentration which leads to larger leakage current. Taking an approximation of the leakage current as

$$J \propto \exp\left(-\frac{E_{form}(V_N)}{k_B T}\right) \times \exp\left(-\frac{-e\phi_{t_4}}{k_B T}\right), \tag{6}$$

we considered the interaction of these two factors and obtained the normalized P-F emission leakage current J/J_0, where J_0 is the leakage under a stress-free condition. From the results shown in Fig. 5(d), it can be concluded that the leakage current of $Al_{0.6875}Sc_{0.3125}N$ increases with increasing compressive in-plane stress. From the experimental results in Figs. 1 and 2, it can be observed that the measured leakage current at the wafer edge with an in-plane stress of approximately -2300 MPa (corresponding to a strain of -0.008) is about 3.7-5.5 times higher than that at the wafer center with a stress of around -800 MPa (corresponding to a strain of -0.003). This measured current ratio is consistent with the theoretical estimation presented in Fig. 5(d). Additionally, when $Al_{0.6875}Sc_{0.3125}N$ undergoes increasing tensile strain, $e\phi_{t_4}$ decreases rapidly, which results in the increase of leakage current by decreasing $e\phi_{t_4}$ nearly canceling out the decrease of leakage current by increasing $E_{form}(V_N)$. As shown in Fig. 5(d), the leakage current is less sensitive to tensile in-plane stress, which requires further exploration in future experiments. In terms of film optimization, the results in Fig. 5(d) indicate that the lowest leakage current is achieved with neutral in-plane stress in the thin film.

To verify the V_N-based leakage mechanism, it's critical to detect and control the V_N in AlScN ferroelectric thin films. However, due to the low atomic number of Nitrogen, it's a challenging task to detect the V_N directly. Recently, scanning transmission electron microscopy (STEM) was implemented to observe and quantify real-time polarization switching in $Al_{0.94}B_{0.06}N$, which is a similar ferroelectric wurtzite to AlScN, at the atomic scale[57]. Based on differentiated differential phase contrast (dDPC) STEM images, both Al(B) and N can be identified and determined with atomic-column positions. This method should enable the detection of V_N in both AlScN and other ferroelectric wurtzite materials. Controlling the V_N could be more feasible with an accurate detecting method for V_N in AlScN, by adjusting the fabrication depositions, which lead to changes in chemical potentials and defect formation energies.

In summary, the stress effect on the leakage current of ferroelectric $Al_{0.7}Sc_{0.3}N$ thin films has been investigated through experiments and theoretical calculations based on DFT. The correlation between in-plane stress and leakage current of $Al_{0.7}Sc_{0.3}N$ was clearly revealed by the similar non-uniform distribution across the wafer. Based on the analysis of formation energies of various defects, V_N is confirmed as the dominant intrinsic defect and acts as the trap center for P-F emission in $Al_{0.6875}Sc_{0.3125}N$ thin film. More importantly, two competitive effects of in-plane stress on leakage have been found, via trap energy barrier $e\phi_{t_4}$ and formation energy $E_{form}(V_N)$, where the former decreases the leakage current with increasing compressive in-plane stress, while the latter increases the leakage. By considering both effects in the P-F emission, the leakage current of $Al_{0.6875}Sc_{0.3125}N$ increases with higher compressive in-plane stress and is quantitatively consistent with the empirical results. In addition, theoretical calculations indicated that the leakage current is insensitive to tensile in-plane stress and the lowest leakage current can be achieved under the stress-free condition. These insights could help in stress engineering for the optimization of ferroelectric $Al_{1-x}Sc_xN$ thin films.

SUPPLEMENTARY MATERIAL

See the supplementary material for the leakage current and local stress distributions of $Al_{0.8}Sc_{0.2}N$ thin film, the TEM and EDX results of the center region and edge region of the $Al_{0.7}Sc_{0.3}N$ thin film wafer, the linear relationship between ln(I/V) and $V^{1/2}$, and the variation of the c lattice constant of $Al_{0.6875}Sc_{0.3125}N$ with different in-plane strain.

ACKNOWLEDGMENTS

The authors from Peking University would like to acknowledge the supports from National Key Research and Development Program (Grant No. 2019YFB2205100) and National Natural Science Foundation of China (Grant No. 92064001). The authors from A*STAR would like to acknowledge the supports from Science and Engineering Research Council of A*STAR (Agency for Science, Technology and Research) Singapore, under Grant No. A20G9b0135. Computational resources were provided by High-performance Computing Platform of Peking University and National SuperComputer Center in Tianjin.

DATA AVAILABILITY STATEMENT

The data that support the findings of this study are available from the corresponding author upon reasonable request.

REFERENCES

[1] R. Turner, P. A. Fuierer, R. Newnham, and T. R. Shrout, Applied Acoustics **41**, 299 (1994).

[2] I. Guy, S. Muensit, and E. Goldys, Applied Physics Letters **75**, 4133 (1999).

[3] A. Zoroddu, F. Bernardini, P. Ruggerone, and V. Fiorentini, Physical Review B **64**, 045208 (2001).

[4] K. Tonisch, V. Cimalla, C. Foerster, H. Romanus, O. Ambacher, and D. Dontsov, Sensors and Actuators A: Physical **132**, 658 (2006).

[5] M. Akiyama, T. Kamohara, K. Kano, A. Teshigahara, Y. Takeuchi, and N. Kawahara, Advanced Materials **21**, 593 (2009).

[6] M. D. Henry, R. Timon, T. R. Young, C. Nordquist, and B. Griffin, ECS Transactions **77**, 23 (2017).

[7] Y. Zhu, N. Wang, G. Chua, C. Sun, N. Singh, and Y. Gu, IEEE Electron Device Letters **38**, 1481 (2017).

[8] R. James, Y. Pilloux, and H. Hegde, in *Journal of Physics: Conference Series*, Vol. 1407 (2019) p. 012083.

[9] J. Zhou, Y. Liu, Q. Xu, Y. Xie, Y. Cai, J. Liu, W. Liu, A. Tovstopyat, and C. Sun, Journal of Microelectromechanical Systems **30**, 677 (2021).

[10] C. Moe, R. Olsson, P. Patel, Z. Tang, M. D'Agati, M. Winters, R. Vetury, and J. Shealy, in *2020 IEEE International Ultrasonics Symposium (IUS)* (2020) pp. 1–4.

[11] Q. Zhang, T. Han, J. Chen, W. Wang, and K. Hashimoto, Diamond and Related Materials **58**, 31 (2015).

[12] M. Akiyama, K. Umeda, A. Honda, and T. Nagase, Applied Physics Letters **102**, 021915 (2013).

[13] L. Kong, J. Zhang, H. Wang, S. Ma, F. Li, Q.-M. Wang, and L. Qin, AIP Advances **6**, 125128 (2016).

[14] P. Mayrhofer, C. Rehlendt, M. Fischeneder, M. Kucera, E. Wistrela, A. Bittner, and U. Schmid, Journal of Microelectromechanical Systems **26**, 102 (2016).

[15]C. Fei, X. Liu, B. Zhu, D. Li, X. Yang, Y. Yang, and Q. Zhou, Nano Energy **51**, 146 (2018).

[16]R. H. Olsson, Z. Tang, and M. D'Agati, in *2020 IEEE Custom Integrated Circuits Conference (CICC)* (2020) pp. 1–6.

[17]D. K. T. Ng, C. P. Ho, L. Xu, W. Chen, Y. H. Fu, T. Zhang, L. Y. Siow, N. Jaafar, E. J. Ng, Y. Gao, *et al.*, Sensors and Actuators B: Chemical **346**, 130437 (2021).

[18]S. Fichtner, N. Wolff, F. Lofink, L. Kienle, and B. Wagner, Journal of Applied Physics **125**, 114103 (2019).

[19]C. Liu, Q. Wang, W. Yang, T. Cao, L. Chen, M. Li, F. Liu, D. K. Loke, J. Kang, and Y. Zhu, in *2021 IEEE International Electron Devices Meeting (IEDM)*, pp. 8.1.1–8.1.4.

[20]M. R. Islam, N. Wolff, M. Yassine, G. Schönweger, B. Christian, H. Kohlstedt, O. Ambacher, F. Lofink, L. Kienle, and S. Fichtner, Applied Physics Letters **118**, 232905 (2021).

[21]P. Wang, D. Wang, N. M. Vu, T. Chiang, J. T. Heron, and Z. Mi, Applied Physics Letters **118**, 223504 (2021).

[22]D. Wang, P. Wang, S. Mondal, S. Mohanty, T. Ma, E. Ahmadi, and Z. Mi, Advanced Electronic Materials **8**, 2200005 (2022).

[23]J. Casamento, K. Nomoto, T. S. Nguyen, H. Lee, C. Savant, L. Li, A. Hickman, T. Maeda, J. Encomendero, V. Gund, A. Lal, J. C. M. Hwang, H. G. Xing, and D. Jena, in *2022 International Electron Devices Meeting (IEDM)*, pp. 11.1.1–11.1.4.

[24]D. Wang, P. Wang, M. He, J. Liu, S. Mondal, M. Hu, D. Wang, Y. Wu, T. Ma, and Z. Mi, Applied Physics Letters **122**, 090601 (2023).

[25]D. K. T. Ng, T. Zhang, L. Y. Siow, L. Xu, C. P. Ho, H. Cai, L. Y. T. Lee, Q. Zhang, and N. Singh, Applied Physics Letters **117**, 183506 (2020).

[26]S. Rassay, D. Mo, and R. Tabrizian, Micromachines **13**, 1003 (2022).

[27]J. Wang, Y. Zheng, and A. Ansari, Physica Status Solidi (RRL) – Rapid Research Letters **15**, 2100034 (2021).

[28]D. Wang, P. Wang, S. Mondal, M. Hu, Y. Wu, T. Ma, and Z. Mi, Advanced Materials **35**, 2210628 (2023).

[29]X. Liu, J. Zheng, D. Wang, P. Musavigharavi, E. A. Stach, R. OlssonIII, and D. Jariwala, Applied Physics Letters **118**, 202901 (2021).

[30]X. Liu, D. Wang, K.-H. Kim, K. Katti, J. Zheng, P. Musavigharavi, J. Miao, E. A. Stach, R. H. Olsson, and D. Jariwala, Nano Letters **21**, 3753 (2021).

[31]G. Schönweger, M. R. Islam, N. Wolff, A. Petraru, L. Kienle, H. Kohlstedt, and S. Fichtner, Physica Status Solidi (RRL) – Rapid Research Letters **17**, 2200312 (2023).

[32]S. Yasuoka, R. Mizutani, R. Ota, T. Shiraishi, T. Shimizu, M. Uehara, H. Yamada, M. Akiyama, and H. Funakubo, ACS Applied Electronic Materials **4**, 5165 (2022).

[33]S. K. Ryoo, K. D. Kim, H. W. Park, Y. B. Lee, S. H. Lee, I. S. Lee, S. Byun, D. Shim, J. H. Lee, H. Kim, Y. H. Jang, M. H. Park, and C. S. Hwang, Advanced Electronic Materials **8**, 2200726 (2022).

[34]M. Pirro, X. Zhao, B. Herrera, P. Simeoni, and M. Rinaldi, Micromachines **13**, 877 (2022).

[35]M. Noor-A-Alam, O. Z. Olszewski, and M. Nolan, ACS Applied Materials & Interfaces **11**, 20482 (2019).

[36]J. Kataoka, S.-L. Tsai, T. Hoshii, H. Wakabayashi, K. Tsutsui, and K. Kakushima, Japanese Journal of Applied Physics **60**, 030907 (2021).

[37]D. Wang, P. Wang, S. Mondal, Y. Xiao, M. Hu, and Z. Mi, Applied Physics Letters **121**, 042108 (2022).

[38]S. Clima, C. Pashartis, J. Bizindavyi, S. R. C. McMitchell, M. Houssa, J. Van Houdt, and G. Pourtois, Applied Physics Letters **119**, 172905 (2021).

[39]K. Yazawa, A. Zakutayev, and G. L. Brennecka, Applied Physics Letters **121**, 042902 (2022).

[40]Q. Wang, S.-X. Go, C. Liu, M. Li, Y. Zhu, L. Li, T. H. Lee, and D. K. Loke, AIP Advances **12**, 125303 (2022).

[41]P. Pobedinskas, J.-C. Bolsée, W. Dexters, B. Ruttens, V. Mortet, J. D'Haen, J. V. Manca, and K. Haenen, Thin Solid Films **522**, 180 (2012).

[42]K. Yazawa, D. Drury, A. Zakutayev, and G. L. Brennecka, Applied Physics Letters **118**, 162903 (2021).

[43]S. Rassay, F. Hakim, C. Li, C. Forgey, N. Choudhary, and R. Tabrizian, Physica Status Solidi (RRL) – Rapid Research Letters **15**, 2100087 (2021).

[44]J. M. Carmona-Cejas, T. Mirea, J. Nieto, J. Olivares, V. Felmetsger, and M. Clement, Materials **16**, 2169 (2023).

[45]A. Zunger, S.-H. Wei, L. Ferreira, and J. E. Bernard, Physical Review Letters **65**, 353 (1990).

[46]S.-H. Wei, L. Ferreira, J. E. Bernard, and A. Zunger, Physical Review B **42**, 9622 (1990).

[47]A. van de Walle, P. Tiwary, M. M. de Jong, D. L. Olmsted, M. D. Asta, A. Dick, D. Shin, Y. Wang, L.-Q. Chen, and Z.-K. Liu, Calphad **42**, 13 (2013).

[48]A. van de Walle, M. D. Asta, and G. Ceder, Calphad **26**, 539 (2002).

[49]J. P. Perdew, K. Burke, and M. Ernzerhof, Physical Review Letters **77**, 3865 (1996).

[50]P. E. Blöchl, Physical Review B **50**, 17953 (1994).

[51]G. Kresse and D. Joubert, Physical Review B **59**, 1758 (1999).

[52]G. Kresse and J. Furthmüller, Physical Review B **54**, 11169 (1996).

[53]K. Momma and F. Izumi, Journal of Applied Crystallography **44**, 1272 (2011).

[54]C. Freysoldt, B. Grabowski, T. Hickel, J. Neugebauer, G. Kresse, A. Janotti, and C. G. Van de Walle, Reviews of Modern Physics **86**, 253 (2014).

[55]R. Batra, T. D. Huan, J. L. Jones, G. Rossetti Jr, and R. Ramprasad, The Journal of Physical Chemistry C **121**, 4139 (2017).

[56]Z. Jiang, C. Paillard, D. Vanderbilt, H. Xiang, and L. Bellaiche, Physical Review Letters **123**, 096801 (2019).

[57]S. Calderon, J. Hayden, S. M. Baksa, W. Tzou, S. Trolier-McKinstry, I. Dabo, J.-P. Maria, and E. C. Dickey, Science **380**, 1034 (2023).